# Large-scale molecular dynamics simulations of glancing angle deposition

Bradley C. Hubartt, Xuejing Liu, and Jacques G. Amar
*Department of Physics & Astronomy*
*University of Toledo, Toledo, Ohio 43606, USA*
(Dated: December 23, 2012)

While a variety of methods have been developed to carry out atomistic simulations of thin-film growth at small deposition angles with respect to the substrate normal, due to the complex morphology as well as the existence of multiple scattering of depositing atoms by the growing thin-film, realistically modeling the deposition process for large deposition angles can be quite challenging. Accordingly, we have developed a computationally efficient method based on the use of a single graphical processing unit (GPU) to carry out molecular dynamics (MD) simulations of the deposition and growth of thin-films via glancing angle deposition. Using this method we have carried out large-scale MD simulations, based on an embedded-atom-method potential, of Cu/Cu(100) growth up to 20 monolayers (ML) for deposition angles ranging from 50° to 85° and for both random and fixed azimuthal angles. A variety of quantities including the porosity, roughness, lateral correlation length, average grain size, strain, and defect concentration are used to characterize the thin-film morphology. For large deposition angles ($\theta \geq 80^o$) we find well-defined columnar growth while for smaller angles, columnar growth has not yet set in. In addition, for $\theta = 70^o - 85^o$ the thin-film porosity and columnar tilt angles (for fixed azimuthal angle $\phi$) are in reasonable agreement with experiments. We also find that for both random and fixed $\phi$ the average strain is initially compressive but becomes tensile after the onset of columnar growth, in good qualitative agreement with recent experimental observations. Our results also indicate that for large deposition angles a variety of complex dynamical processes including coalescence, large-scale collective events, and budding play a key role in determining the evolution of the surface morphology and microstructure.

PACS numbers: 68.55.-a, 81.15.Aa, 81.15.-z, 81.07.-b

## I. INTRODUCTION

Glancing angle deposition (GLAD) is a commonly used physical vapor deposition technique which may be used to produce sculptured thin-films with a variety of different morphological, electrical, and chemical properties.[1,2] In this technique, atoms are typically deposited at a large angle $\theta$ with respect to the substrate normal while the azimuthal angle $\phi$ may either be held fixed to produce tilted nanocolumns, continuously rotated to produce vertical columnar growth, or manipulated in a more complicated manner to produce nanostructures such as nanosprings. As a result glancing-angle deposited thin-films have potential applications[2,3] in a variety of different areas including sensors, hydrogen storage, antireflective coatings, fuel-cells, magnetic storage devices, and solar cells.

Due to the dominant influence of shadowing on the thin-film morphology, a variety of simplified models[4,5] (corresponding to growth on a simple-cubic lattice) have been successfully used to model the dependence of the overall thin-film morphology on deposition angle. However, a variety of other important aspects such as the crystalline structure, grain boundaries, and defects, as well as deposition-triggered events[6,7] and concerted activated events are not included in these simulations. In addition, while a kinetic Monte Carlo model (ADEPT) for polycrystalline Al growth[8] has recently been developed which approximately takes into account grain orientation and grain boundaries by using multiple lattices, due to the lattice restriction this model does not take into account strain effects during growth, deposition-triggered events,[6,7] or concerted activated events.

While limited in time-scales, molecular dynamics (MD) simulations can realistically take into account all of these aspects of glancing-angle deposition thin-film growth. However, due to the existence of multiple scattering at large deposition angles, carrying out molecular dynamics simulations of glancing angle deposition over extended length-scales can be quite challenging. Accordingly, we have developed a computationally efficient method (based on the use of a single graphical processing unit or GPU) to simulate the deposition process at large deposition angles.

Using this method we have carried out large-scale MD simulations of GLAD of Cu/Cu(100) at 300 K, in order to study the dependence of the morphology and crystal structure on deposition angle both with and without substrate rotation. In agreement with experiments, for large deposition angles ($\theta \geq 80^o$) we find well-defined columnar growth with vertical (tilted) columns for random (fixed) $\phi$, while for $\theta = 70^o - 85^o$ the thin-film porosity and columnar tilt angles (for fixed $\phi$) are in reasonable agreement with experiments. In addition, we find that while the average strain is initially compressive for both random and fixed $\phi$, it becomes tensile after the onset of columnar growth, in good qualitative agreement with recent experimental observations.[9] Our results also indicate that even on MD time-scales a variety of complex dynamical processes including coalescence, large-scale collective events, and budding play a key role in determining the evolution of the surface morphology and microstructure.

This paper is organized as follows. In Sec. II we first

discuss our simulation methods and parameters as well as the quantities measured. We then present our results for the evolution of the thin-film morphology and microstructure as a function of film thickness and deposition angle, for the case of both fixed and random azimuthal angle in Sec. III. Finally, we summarize our results in Sec. IV.

## II. SIMULATIONS

### A. Simulation Parameters and Methods

In our simulations we have used an embedded-atom-method (EAM)[10] potential for Cu developed by Mishin et al.[11] which has been parameterized to reproduce the *ab initio* values of stacking fault and twin formation energies. In order to minimize finite-size effects we have used a relatively large system size corresponding to an initial square Cu(100) substrate of width $L = 80\ a$ (where $a$ is the lattice constant of Cu) with 3 (bottom) fixed layers, 5 (middle) constant-temperature layers, and 2 (top) moving layers. A Langevin thermostat with a friction coefficient of $10^{12}$ s$^{-1}$ was used for the constant temperature layers while periodic boundary conditions were assumed parallel to the substrate. In order to study the dependence on deposition conditions, we have carried out simulations for deposition angles $\theta$ ranging from $\theta = 50^o$ to $\theta = 85^o$, as well as for both fixed azimuthal angle $\phi$ (corresponding to deposition along the [110] direction) and random $\phi$ (corresponding to a rotating substrate). Our simulations were carried out at 300 K while a total of 20 monolayers (ML) corresponding to 256,000 atoms were deposited in each case. In order to maximize computational efficiency, our simulations were carried out using a single graphical processing unit or GPU along with the public domain software HOOMD-blue,[12–14] which provides an efficient implementation of molecular dynamics on GPUs for a variety of different potentials.

In our simulations 1/200 ML (corresponding to 64 atoms) was deposited in each deposition step or cycle, while to avoid interactions a sublattice was used (see Fig. 1). In particular, the area above the growing film was divided into an 8×8 grid which was further divided into 4 sublattices, A,B, C, and D (see Fig. 1). At the beginning of each deposition cycle one of the sublattices is randomly selected and within each grid an initial $(x, y)$ coordinate is randomly selected within the corresponding sublattice. The initial $z$-coordinate was determined by adding the cutoff distance to the highest $z$-coordinate in the film. Each depositing atom was then "launched" with the appropriate deposition and azimuthal angle, with an initial kinetic energy of 0.2 eV (corresponding to $K_i = \sqrt{2k_BT_m}$ where $T_m$ is the melting temperature of Cu). We note that the use of a grid with sublattices ensures that the initial distance between depositing atoms is larger than $5a$ or approximately $18\mathring{A}$.

In order to efficiently take multiple scattering of depositing atoms by the growing film into account, in each deposition cycle an alternating sequence of processes consisting of ballistic deposition of all depositing atoms until they are within a cutoff distance from the substrate, followed by molecular dynamics simulations of the entire system for 1000 MD steps is carried out. In order to ensure accurate evolution during deposition, a relatively short time-step (0.41 fs) is used. This sequence of ballistic deposition and molecular dynamics was repeated until all of the depositing atoms were able to satisfy a landing criterion for two 1000 MD-step sequences. We note that to be considered to have 'landed' an atom was required to move less than $1.5\mathring{A}$ from its initial position (roughly 60% of the nearest-neighbor distance for Cu) at the end of two successive 1000 MD-step sequences. Once all depositing atoms have landed, an additional 5000 MD steps were performed. We then increased the time-step to 3.2 fs and continued performing MD of the entire system until a total MD time of 16.4 ps had elapsed during each deposition cycle (corresponding to a deposition rate of 0.3 ML/ns). We note that when running on a single CPU each of our simulations would have required over 15,000 hours of CPU time which is significantly larger than the few hundred hours required when using a GPU.

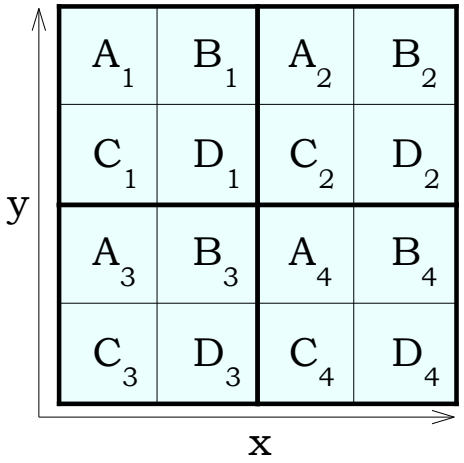


FIG. 1: Schematic showing $2 \times 2$ portion of $8 \times 8$ grid (along with A,B,C, and D sublattices) used to determine initial $x, y$ coordinates of depositiing atoms in each cycle.

### B. Quantities Measured

In order to analyze the surface morphology we have measured a variety of quantities, including the root-mean-square height fluctuation or roughness

$$w = \frac{1}{N_c^{1/2}} \left[\Sigma_{i=1}^{N_c}(h(\mathbf{r_i}) - \bar{h})^2\right]^{1/2} \quad (1)$$

where $h(\mathbf{r_i})$ is the maximum height $z_i$ above the substrate of all the atoms in column $i$ at position $\mathbf{r_i} = (x_i, y_i)$ along the substrate plane and $N_c = 160^2$ is the number

of columns. Here we have mapped the $(x, y)$ coordinates of each atom to the nearest point on a $160 \times 160$ square grid of box-size $a/2$ and $\bar{h}$ is the average film height. In addition, we have calculated the porosity,

$$P = 1 - \frac{N_{dep} V_{atom}}{h_{max} L^2} \tag{2}$$

where $h_{max}$ is the maximum height of the film above the substrate, $N_{dep}$ is the total number of atoms deposited, and $V_{atom} = a^3/4$ is the volume per atom in an fcc crystal. For the case of random azimuthal angle (corresponding to vertical columnar growth) we have also calculated the circularly-averaged height-height correlation function

$$G(r) = \langle \tilde{h}(0)\tilde{h}(r) \rangle_C \tag{3}$$

where $\tilde{h}(r) = h(r) - \bar{h}$ and the brackets denote a circular average over all directions, as well as the lateral correlation length $\xi = r_{min}$ where $G(r_{min})$ is the minimum value of $G(r)$.

In order to analyze the thin-film microstructure, we have also measured a variety of other quantities. In particular, in order to distinguish between bulk, surface, and/or defect atoms for each atom $i$ of the film we have calculated the centrosymmetry parameter $\rho_{CS}(i)$, defined by,[15]

$$\rho_{CS}(i) = \frac{1}{a} \Sigma_{j=1} |\vec{R}_j + \vec{R}_{j+6}|^2 \tag{4}$$

where $R_j$ and $R_{j+6}$ are the vectors corresponding to the six pairs of most opposite nearest atoms. Using this parameter, atoms were then classified as either bulk atoms ($\rho_{CS} < 0.03$), dislocation atoms ($0.03 < \rho_{CS} < 0.075$), stacking fault atoms ($0.075 < \rho_{CS} < 0.5$), or surface atoms ($\rho_{CS} > 1.25$). By counting the number of "bulk" atoms surrounded by defects, the average grain-size and grain-size distribution were also determined. In addition, we estimated the vacancy density by calculating the volume of empty regions surrounded by surface atoms within a grain, and dividing by the average volume per atom. In order to study the effects of deposition conditions on strain, we have also calculated the average strain $\bar{\epsilon} = \langle \epsilon_i \rangle$ as a function of film-thickness where $\epsilon_i = \frac{1}{a_1} \Sigma_{j=1}^{N} (|\mathbf{r_j} - \mathbf{r_i}|/N - a_1)$ is the local strain at atom $i$, $a_1$ is the nearest-neighbor distance of bulk Cu, and the sum is over the total number $N$ of nearest-neighbors of atom $i$ (corresponding to all atoms whose distances are within 20% of the bulk nearest-neighbor distance).

## III. RESULTS

### A. Morphology

Fig. 2 shows typical pictures of the surface morphology at coverage 15 ML for the case of random azimuthal angle. As can be seen, for moderate deposition angles $\theta = 50^o$ (not shown) and $60^o$ columnar growth has not yet set in, although the surface morphology becomes increasingly rough with increasing coverage. However, for larger deposition angles $\theta \geq 70^o$ a well-defined vertical columnar structure is beginning to develop, which becomes more pronounced with increasing deposition angle and film-thickness.

In contrast, for fixed azimuthal angle (see Fig. 3) and moderate deposition angles $\theta = 50^o - 60^o$, ridge-like behavior with (100) cliffs running perpendicular to the deposition direction may be seen, as was previously found in Ref. 7. However, for larger deposition angles ($\theta = 70^o, 80^o$, and $85^o$) a well-defined columnar structure is again observed, which becomes more pronounced with increasing deposition angle and film-thickness. In this case the columns are tilted in the deposition direction. Accordingly, we have measured the average tilt angle $\beta$ corresponding to the angle between columns and the substrate normal at $t = 20ML$ for $\theta = 70^o, 80^o$, and $85^o$ to be $42.8^o \pm 8.3^o, 49.33^o \pm 7^o$, and $39.6^o \pm 11.6^o$ respectively. Due to the existence of significant finite size effects for $\theta = 85^o$ at higher coverage (see Fig. 3) the value is somewhat lower than expected. However, our two other values are close to the tilt angles measured in GLAD experiments by Suzuki and Taga[5] e.g. $\beta = 43^o$ at $\theta = 70^o$ for both $Ta_2O_5$ and $TiO_2$, and $\beta = 53^o$ at $\theta = 82^o$ for $Ta_2O_5$.

We note that for both random and fixed $\phi$, shadowing of smaller columns by larger columns as well as coalescence of nearby columns can be observed. Both of these processes lead to coarsening as the film-thickness increases. In particular, for $\theta = 85^o$ with random $\phi$ (see Fig. 2), as the coverage increases from 10 ML to 15 ML the three columns in the bottom right corner of the system merge to form one column. In addition, for the case of random azimuthal angle, "budding" or splitting of a single column into two columns is also observed due to "twin" (111) facet formation (see back middle portion of pictures for $\theta = 85^o$).[16]

Fig. 4 shows our results for the porosity $P$ (averaged over $12 - 20$ ML) as a function of deposition angle. As can be seen, the porosity increases significantly with increasing deposition angle although there is little difference between the results for fixed and random $\phi$. Also shown (dashed lines) are fits to experimental results of Poxson et al[17] for $SiO_2$ and indium tin oxide (ITO) for fixed azimuthal angle, where we have used the Poxson et al[17] fitting form $P_{exp} = \frac{\theta \tan\theta}{c + \theta \tan\theta}$ with $c = 3.17$ (3.55) for $SiO_2$ (ITO) respectively. For large deposition angles there is good agreement between our simulation results and experiments due to the fact that the effects of shadowing dominate in this case. As can be seen in the inset to Fig. 4 for these angles the porosity saturates relatively quickly after the first few layers. However, for smaller deposition angles our porosity results for Cu/Cu(100) are somewhat higher than the experimental values for $SiO_2$ and ITO, perhaps because fully columnar behavior has not yet been reached for these angles in our simulations.

The thin-film density as a function of height after 20

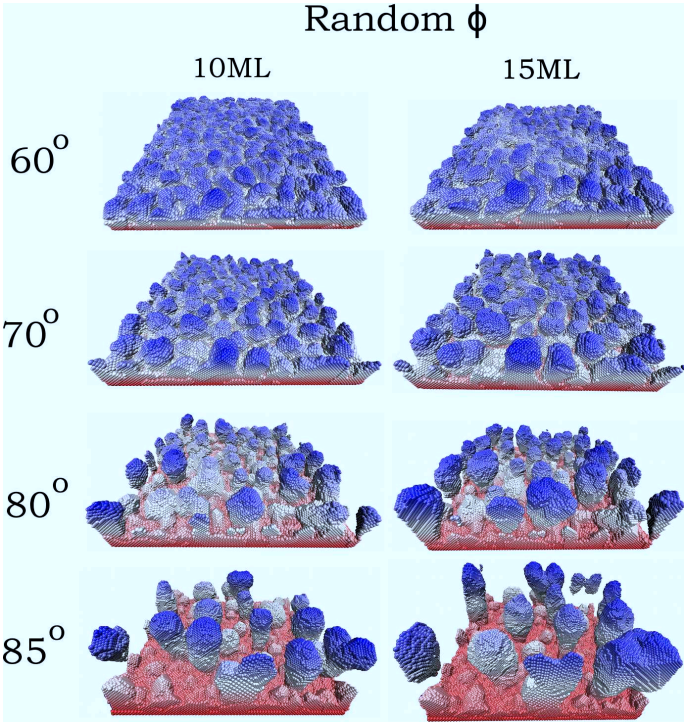


FIG. 2: Thin-film configurations for random azimuthal angle at 10 and 15 ML for $\theta = 60^o, 70^o, 80^o$, and $85^o$. Atoms are colored according to height above substrate.

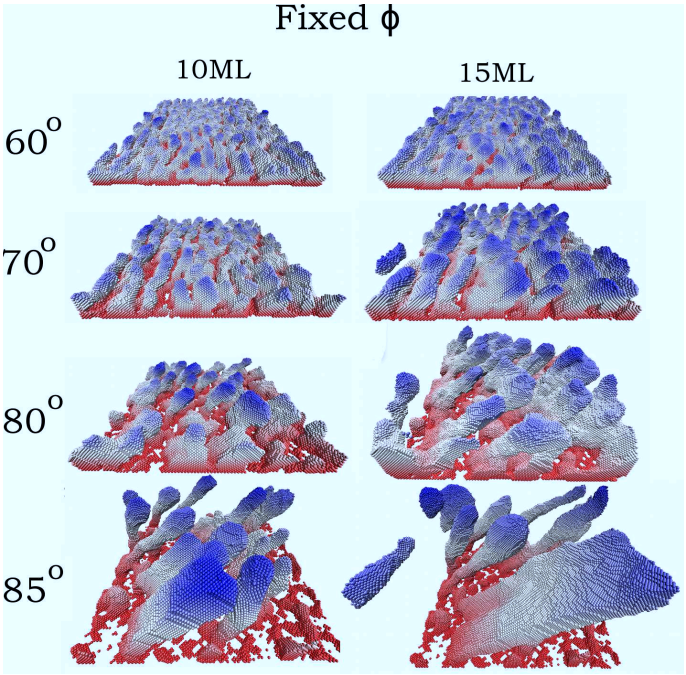


FIG. 3: Thin-film configurations for fixed azimuthal angle at 10 and 15 ML for $\theta = 60^o, 70^o, 80^o$, and $85^o$.

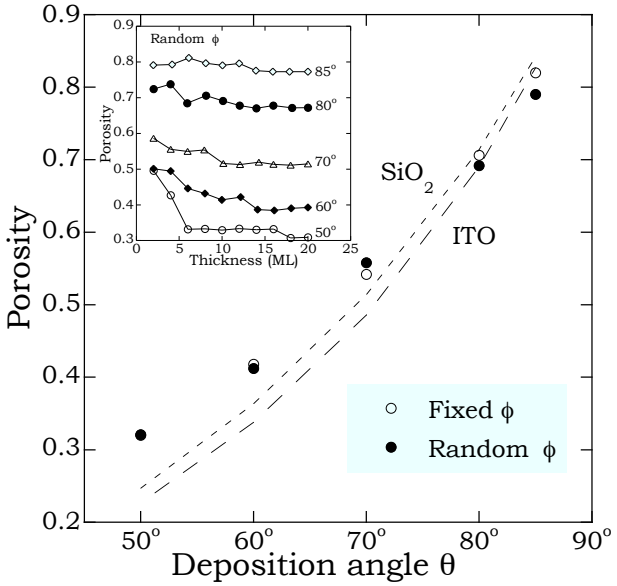


FIG. 4: Comparison of thin-film porosity obtained in simulations (symbols) with fits to experimental results (dashed lines) for $SiO_2$ and ITO. Inset: Porosity as a function of film thickness for random $\phi$.

ML, is shown in Fig. 5 for all deposition angles for the case of random $\phi$. (Similar results have been obtained for fixed $\phi$ but are not shown for brevity.) As can be seen, for $\theta = 80^o$ and $85^o$ there is a well-defined region of constant density corresponding to columnar growth, while for smaller deposition angles ($\theta = 50^o, 60^o$ and $70^o$) for which columnar growth is not yet fully defined by 20 ML, there is no well-defined region of constant density. Consistent with our porosity results the maximum film height increases with increasing deposition angle.

In order to gain a better understanding of the surface morphology, we have also measured the roughness $w$ as a function of film-thickness. As can be seen in Fig. 6, for random $\phi$ the surface roughness increases approximately linearly, as expected for columnar growth. However, for fixed $\phi$ the growth exponent $\beta$ (where $w \sim t^\beta$ and $t$ is the film thickness) is less than 1 for small deposition angles, but approaches 1 for $\theta = 80^o$ and $85^o$. We note however, that for $\theta = 85^o$ the surface roughness is somewhat reduced for $t > 15$ ML due to finite-size effects.

The circularly-averaged lateral correlation length $\xi$ for random $\phi$ is shown in Fig. 7 as a function of deposition angle and film-thickness. For large deposition angles, the coarsening exponent $n$ (where $\xi \sim t^n$) is approximately 1/2 in good agreement with previous GLAD simulation results using a simple-cubic lattice model in the absence of diffusion.[18,19] The large value of the coarsening exponent is also consistent with the large amount of shadowing and coalescence (discussed in more detail below) at high deposition angles. However, for smaller deposition angles, the coarsening exponents are significantly smaller ($n \simeq 0.2 - 0.33$) and are consistent with the values obtained in simulations with surface diffusion.[19] In contrast,

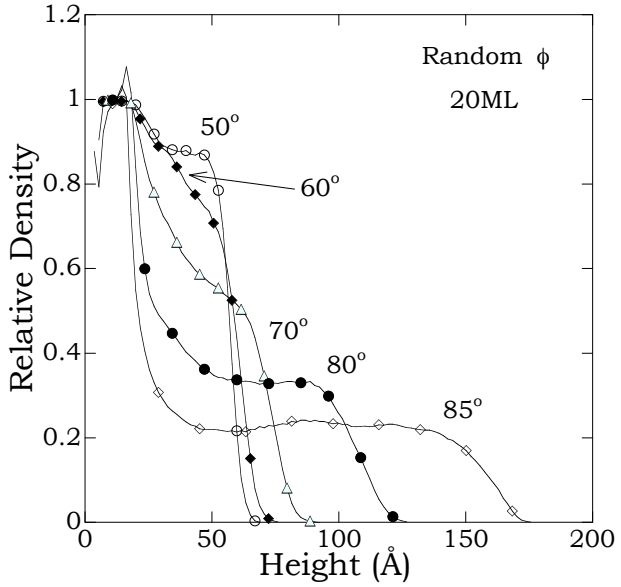


FIG. 5: Density profile (normalized to bulk density) of simulated films for random $\phi$ at 20 ML coverage.

we find that while the surface atom fraction (not shown) increases with deposition angle, the surface area growth exponent $\delta \simeq 0.5$ (where $S \sim t^{\delta}$ is the number of surface atoms) is independent of deposition angle.

### B. Microstructure and Strain

In order to study the microstructure we have used the centrosymmetry parameter to classify film atoms as either surface atoms, defect atoms (corresponding to stacking faults and/or partial dislocations), or bulk atoms. Fig. 8(a) shows a typical picture of the grain structure for the case of $\theta = 85^o$ and random $\phi$ at $t = 15ML$. (Note that the configuration in this picture is the same as that shown in Fig. 2 but viewed from behind.) In this picture only the bulk atoms are shown and have been colored to distinguish between different grains while the gaps between grains correspond to stacking fault atoms which have been removed from the image. In this case, approximately 90% of the deposited atoms do not belong to the original (yellow) "substrate" grain. (In contrast, for $\theta = 50^o$ and 15 ML, only approximately 35% of the deposited atoms correspond to defects or bulk atoms which do not belong to the substrate grain.) Fig. 8(b) shows just the stacking fault atoms for this configuration. As can be seen there are well-defined stacking fault planes. This is consistent with our observation that for all deposition angles there are a relatively large number of (100) and (111) facets, while the ratio of (111) facet atoms to (100) facet atoms increases with deposition angle.

Fig. 9 shows the evolution of the average (non-substrate) grain size (corresponding to the average number of atoms in a grain) as a function of coverage for the

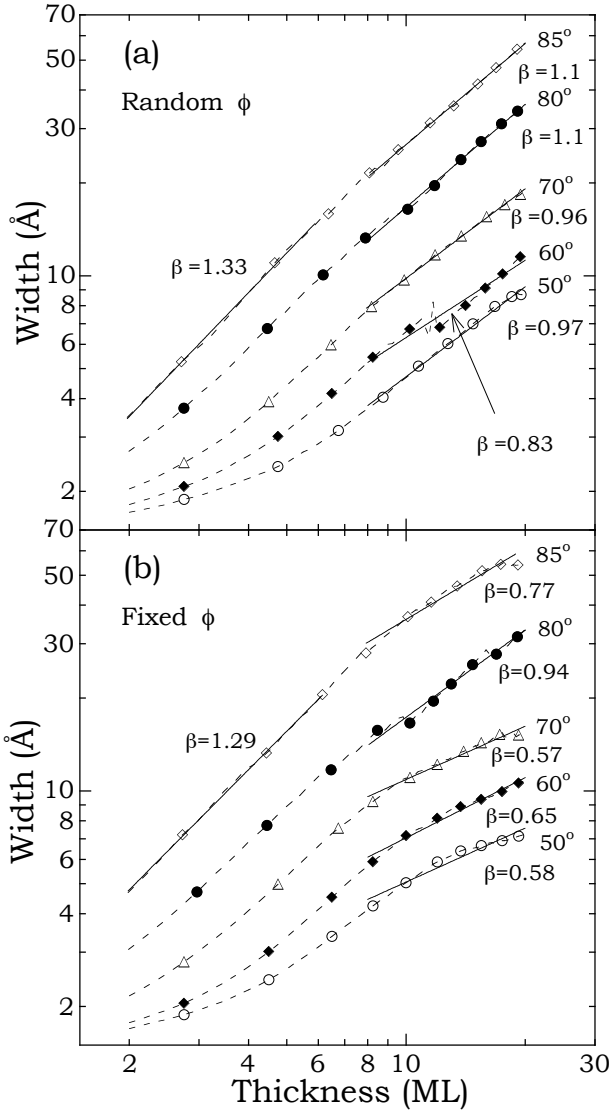


FIG. 6: Surface width as a function of film thickness for (a) random $\phi$ and (b) fixed $\phi$.

case of random $\phi$ and different deposition angles. As can be seen, both the average non-substrate grain size as well as the total number of grains (see inset) increase rapidly with both film thickness and deposition angle. Similar results have also been obtained for fixed $\phi$. However, due to the fact that both shadowing and coalescence are more significant for fixed $\phi$, in this case the average grain size is significantly larger than for random $\phi$ while the number of non-substrate grains is significantly smaller.

In order to more completely analyze the microstructure we have also calculated the vacancy volume fraction for random $\phi$ as shown in Fig. 10. As can be seen, while the vacancy fraction increases with deposition angle, it appears to saturate at a value of approximately 0.001 which is independent of deposition angle. This very small vacancy density may be explained by the presence of deposition-induced events, which have been previously

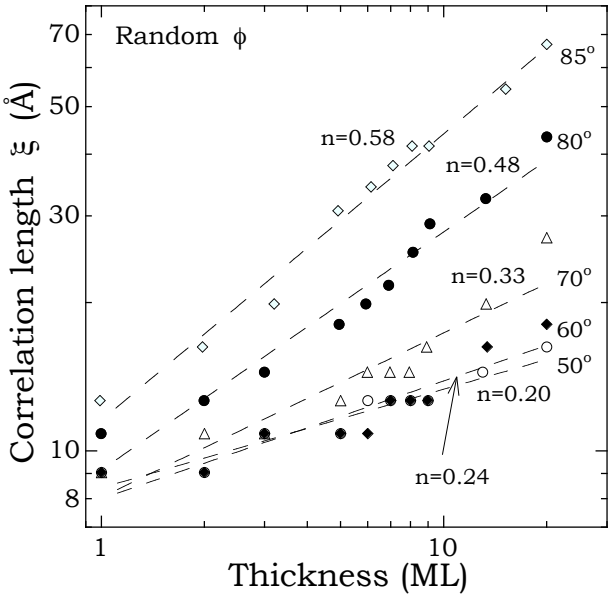


FIG. 7: Lateral correlation length as a function of film thickness for random $\phi$.

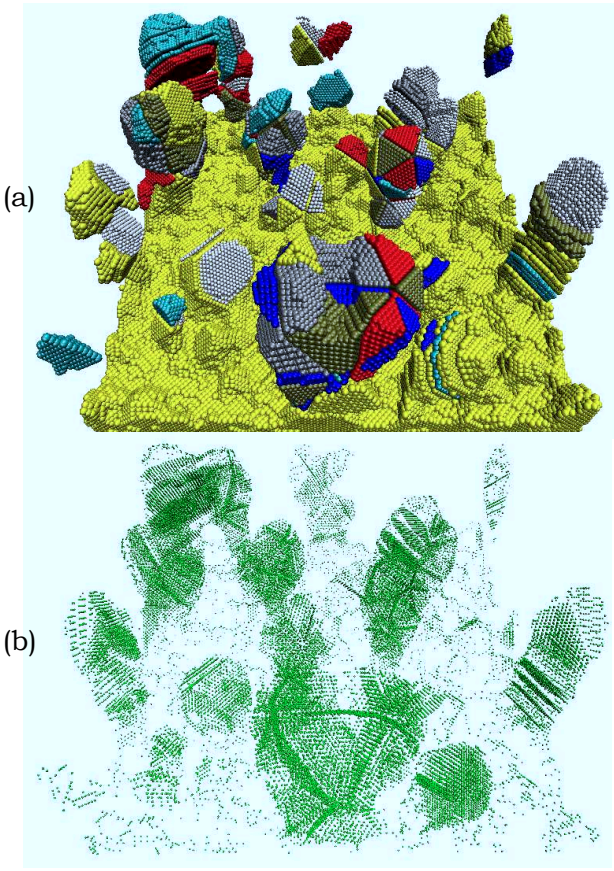


FIG. 8: (a) Grain structure of simulated film for $\theta = 85^o$ and random $\phi$, at $t$ = 15 ML. Only bulk atoms are shown and each grain is colored differently from its neighbors but not uniquely. (b) Same configuration as in (a) but only stacking fault atoms are shown.

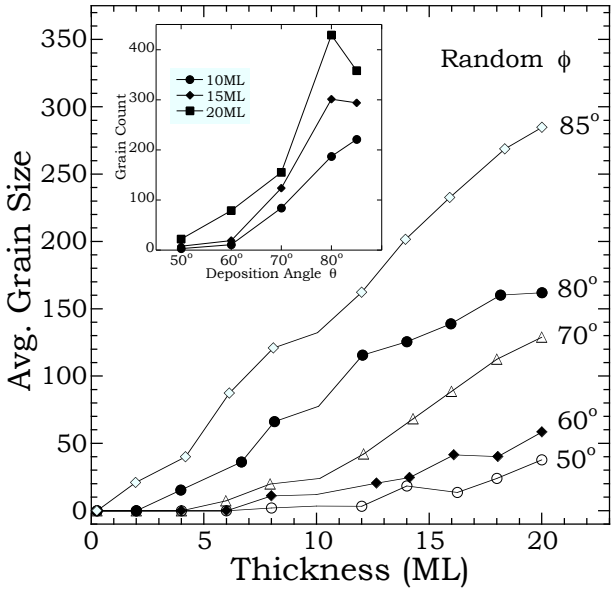


FIG. 9: Average grain size (not including large substrate grain) as function of film thickness for different deposition angles $\theta$ and random $\phi$. Inset shows grain count at 10, 15, and 20 ML as function of deposition angle.

shown[7] to eliminate vacancies even in the absence of thermally activated events. Similar results (not shown) were also obtained for the case of fixed $\phi$ and in this case the vacancy fraction was approximately the same. Interestingly, the vacancy density $v$ exhibits an approximate power-law dependence on thickness of the form $v \sim t^{\gamma}$ starting at a few ML up until saturation. The exponent $\gamma$ is independent of deposition angle and is approximately given by 1.5 (1.3) for random (fixed) $\phi$. We note that this power-law behavior extends over a larger range of coverage for smaller deposition angles, due to the slower rate of vacancy formation. In contrast, the total defect atom density including dislocations and stacking faults is more than two orders of magnitude larger (see inset). In addition, while it increases rapidly in the first 2 ML for all deposition angles, for large coverage it depends strongly on the deposition angle.

We have also measured the average strain as a function of coverage and deposition angle. As can be seen in Fig. 11 for the case of random $\phi$, while the strain is initially compressive for all deposition angles, for large deposition angles ($\theta = 80^o$ and $85^o$) it becomes tensile at larger thicknesses corresponding to columnar growth. Interestingly, for $\theta \geq 70^o$, the maximum compressive strain appears to correspond to the onset of a columnar morphology during the growth. Similar results have also been obtained (not shown) for the case of fixed azimuthal angle. The transition from compressive to tensile strain at the onset of columnar growth is qualitatively similar to the behavior obtained previously in Ref. 9 in sputter-deposition experiments on Be growth with and without substrate bias.

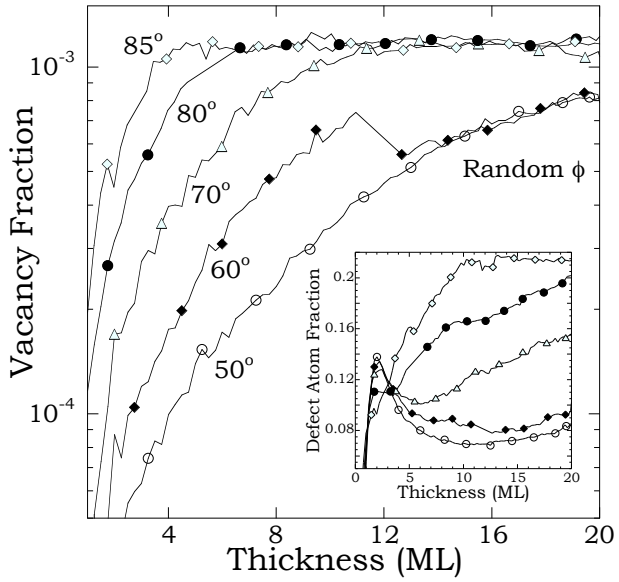


FIG. 10: Vacancy fraction as function of film-thickness and deposition angle for random $\phi$. Total defect atom fraction is shown in inset.

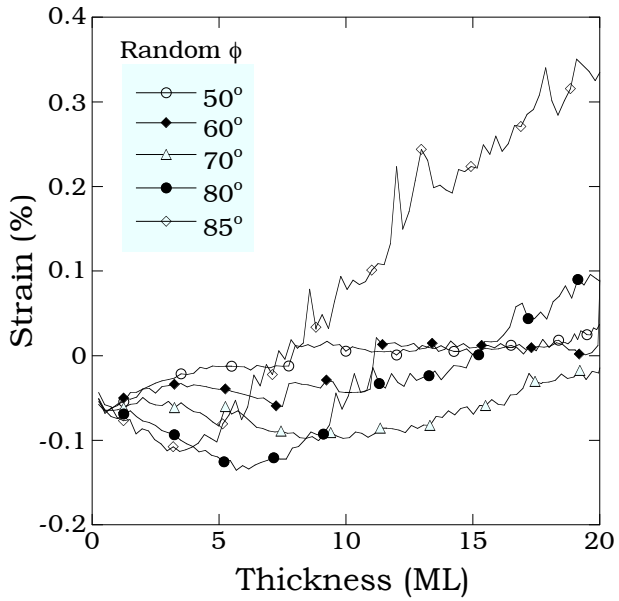


FIG. 11: Average strain as function of film-thickness and deposition angle for random $\phi$.

### C. Large-scale rearrangement, coalescence and budding

As previously noted, in the case of columnar growth ($\theta \geq 70^o$), the coalescence of nearby columnar structures plays an important role in determining the evolution of the surface morphology. In particular, a careful examination of the evolution of the surface morphology after columnar structures have formed, indicates that due to deposition-induced fluctuations as well as the large defect

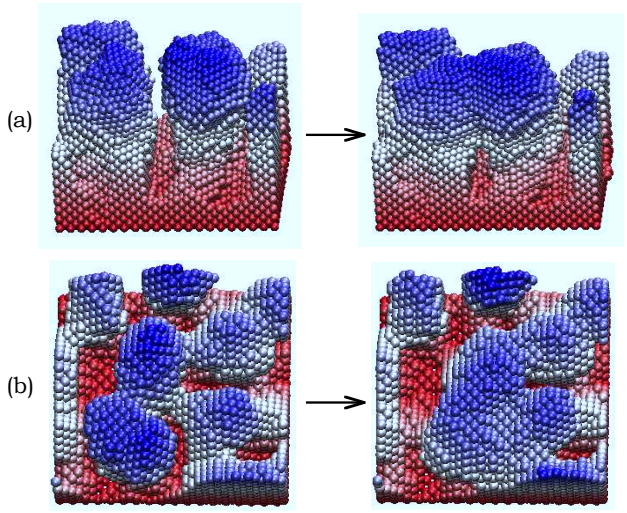


FIG. 12: Large-scale coalescence events for random $\phi$ and $\theta = 70^o$ which occur at approximately (a) 16.75 ML and (b) 11.5 ML. In each case, the interval between snapshots corresponds to 0.25 ML.

density (see inset of Fig. 10) large-scale rearrangements continually occur leading to 'wiggling' of columns. In addition, when two columns or grains approach within a cutoff distance from one another, then rapid coalescence occurs as a result of large-scale collective motions which include rotation and tilting (see Fig. 12). In order to understand this in more detail we have carried out annealing simulations for the case of random $\phi$ and $\theta = 70^o$ both with and without deposition, and at both 77 K and 300 K. Surprisingly, we find that while deposition-induced events may enhance the fluctuations which lead to coalescence, coalescence occurs both with and without deposition and at both high and low-temperatures. However, at low temperature less atomic re-arrangement is observed after coalescence.

In contrast to the large-scale rearrangement and coalescence of nearby columns, which enhance coarsening, we have also found that in the case of random azimuthal angle, splitting and/or budding of columns may also occur as shown in more detail in Fig. 13. Similar budding behavior has also been seen experimentally[16] and has been explained[16] as due to the existence of twin (111) facets combined with shadowing and the existence of a 3D Ehrlich-Schwoebel barrier[20–22] to interfacet diffusion. As can be seen by the orientation of the stacking faults shown in the front-center of Fig. 8(b), the budding appears to be associated with twin (111) facets which form spontaneously during growth.

## IV. DISCUSSION

We have developed a computationally efficient method to carry out molecular dynamics simulations of the deposition and growth of thin-films for large deposition angle. Since the entire system is included at every stage

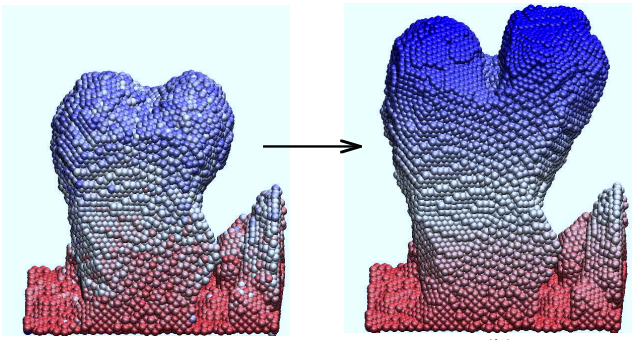


FIG. 13: Sequence of pictures at (a) 13.5 ML and (b) 17.25 ML showing budding for $\theta = 85^o$ with random $\phi$. Color scheme indicates height of atoms above substrate.

of the simulation, multiple scattering events which occur at large deposition angles are easily taken into account. Using this method we have carried out large-scale simulations of Cu/Cu(100) growth for deposition angles ranging from 50° to 85° for both fixed and random azimuthal angle with a deposition rate corresponding to 0.3 ML/ns.

In agreement with experiments, for large deposition angles ($\theta \geq 80^o$) we find well-defined columnar growth with vertical (tilted) columns for random (fixed) $\phi$. For fixed $\phi$ and $\theta = 70^o - 85^o$ we have also found reasonable agreement between the measured tilt angle and experiments on $Ta_2O_5$ and $TiO_2$ growth by Suzuki and Taga.[5] In addition, for large deposition angles our results for the thin-film porosity were found to be in excellent agreement with recent experimental values.[9] In this case for both random and fixed $\phi$ we have also found that while the strain is initially compressive, it becomes tensile after the onset of columnar growth for large deposition angles, in good qualitative agreement with the behavior obtained previously by Zepeda-Ruiz et al[9] in sputter-deposition experiments on Be growth with and without substrate bias.

In contrast, for smaller deposition angles ($\theta = 50^o$ and $60^o$) columnar growth is not observed up to the maximum coverage (20 ML) studied in our simulations. Instead, primarily ridge-like behavior is observed in good agreement with previous MD and temperature-accelerated dynamics results,[7] while the average strain remains compressive. For these angles our simulated porosities are somewhat higher than experimental values, perhaps due to the fact that columnar growth has not yet set in at these thicknesses.

For all deposition angles, we find large values of the surface roughness growth exponent $\beta$, where $\beta \simeq 1$ for the case of random $\phi$ while $\beta \simeq 0.6 - 1$ for fixed $\phi$. In addition, for random azimuthal angle and large deposition angles ($\theta = 80^o$ and $85^o$) the coarsening exponent $n \simeq 1/2$ is in good agreement with previous GLAD simulation results using a simplified cubic-lattice model without diffusion.[19] However, for smaller deposition angles, the corresponding coarsening exponents ($n \simeq 0.2 - 0.33$) are consistent with GLAD simulation results previously obtained in the presence of surface diffusion.[19] One possible explanation for this difference in the coarsening behavior may be the existence of relaxation processes which only occur at small length-scales.

Due to the large deposition rate in our MD simulations, a large number of stacking faults are also observed leading to the formation of numerous grains and grain boundaries. In addition, the number of defects and grains, as well as the average non-substrate grain size increase with increasing deposition angle. In contrast, due to deposition-induced events the vacancy density remains extremely small (less than 0.1%) for all deposition angles.

While these results reveal a number of interesting features (such as the existence of defects, grain boundaries, low vacancy density, and a transition from compressive to tensile strain) which can only be properly studied using atomistic models, our simulations have also revealed two other important and interesting processes which may occur during glancing-angle deposition. In particular, our simulation results indicate that deposition fluctuations as well as large-scale re-arrangement events lead to 'wiggling' of columns for large deposition angles. In addition, when two columns approach within a cutoff distance from one another, further large-scale re-arrangements occur followed by rapid coalescence, thus enhancing the coarsening process. We have also found that in the case of large deposition angle with random $\phi$, splitting and/or budding of columns may also occur. This has been previously observed experimentally[16] and explained as a result of the formation of twin (111) facets combined with shadowing as well as a 3D Ehrlich-Schwoebel barrier[20–22] to diffusion from one facet to the other. We note that in our simulations this budding occurs naturally, in contrast to previous MD simulations[16] in which the growth of a single column with twinned facets was studied.

In conclusion, our simulations demonstrate that while simplified lattice models may provide a good description of some of the morphological features and processes in glancing-angle deposition, atomistic simulations are required in order to obtain a more complete understanding. In the future it would be interesting to combine our "parallel" MD simulations with parallel temperature-accelerated dynamics simulations,[7,23] in order to study the evolution of the thin-film morphology and microstructure over longer time- and length-scales.

### Acknowledgments

This research was supported by NSF grant DMR-0907399 as well as by the University of Toledo Wright Center for Photovoltaic Innovation and Commercialization (PVIC). J.G.A. also received support from the Air Force Research Laboratory under Contract No.FA9453-08-C-0172 as well as a grant of computer time from the Ohio Supercomputer Center.

[1] Y. Zhao, D. Ye, G. Wang, and T. Lu, Proc. SPIE **5219**, 59 (2003).
[2] M. M. Hawkeye and M. J. Brett, J. Vac. Sci. Tech. A **25**, 1317 (2007).
[3] F. Favier, E. C. Walter, M. P. Zach, T. Benter, and R. M. Penner, Science **293**, 2227 (2001).
[4] T. Smy, D. Vick, M.J. Brett, S.K. Dew, A.T. Wu, J.C. Sit, and K. D. Harris, J. Vac. Sci. Tech. A **18**, 2507 (2000).
[5] M. Suzuki and Y. Taga, J. Appl. Phys. **90**, 5599 (2001).
[6] F. Montalenti and A.F. Voter. Phys. Rev. B, **64**, 081401 (2001).
[7] Y. Shim, V. Borovikov, B.P. Uberuaga, A.F. Voter, and J.G. Amar, Phys. Rev. Lett. **101**, 116101 (2008).
[8] J.E. Rubio, M. Jaraiz, I. Martin-Bragado, J.M. Hernandez-Mangas, J. Barbolla, and G.H. Gilmer, J. Appl. Phys. **94**, 163 (2003).
[9] L.A. Zepeda-Ruiz, E. Chason, G.H. Gilmer, Y. Wang, H. Xu, A. Nikroo, and A.V. Hamza, Appl. Phys. Lett., **95**, 151910 (2009).
[10] M.S. Daw and M.I. Baskes, Phys. Rev. B **29**, 6443 (1984).
[11] Y. Mishin, M.J. Mehl, D.A. Papaconstantopoulos, A.F. Voter, and J.D. Kress, Phys. Rev. B **63**, 224106 (2001).
[12] J.A. Anderson, C.D. Lorenz, and A. Travesset, J. Comp. Phys. **227**, 5342 (2008).
[13] http://codeblue.umich.edu/hoomd blue.
[14] I.V. Morozov, A.M. Kazennov, R.G. Bystryi, G.E. Norman, V.V. Pisarev, and V.V. Stegailov, Comp. Phys. Comm. **182**, 1974 (2011).
[15] C.L. Kelchner, S.J. Plimpton, and J.C. Hamilton, Phys. Rev. B **58**, 11085 (1998).
[16] J. Wang, H. Huang, S.V. Kesapragada, and D. Gall, Nanolett. **5**, 2505 (2005).
[17] D.J. Poxson, M. Kuo, F.W. Mont, Y. Kim, X. Yan, R.E. Welser, A.K. Sood, J. Cho, S. Lin, and E.F. Schubert, Mat. Res. Soc. Bull. **36**, 434 (2011).
[18] S. Mukherjee, C.M. Zhou, and D. Gall, J. Appl. Phys. **105**, 094318 (2009).
[19] T. Karabacak, J.P. Singh, Y.P. Zhao, G.-C. Wang, T.-M. Lu, Phys. Rev. B **68**, 125408 (2003).
[20] S.J. Liu, H.C. Huang, and C.H. Woo, Appl. Phys. Lett. **80**, 3295 (2002).
[21] G. Ehrlich and F.G. Hudda, J. Chem. Phys. **44**, 1039 (1966).
[22] R.L. Schwoebel and E.J. Shipsey, J. Appl. Phys. **37**, 3682 (1966).
[23] Y. Shim, J. G. Amar, B.P. Uberuaga, and A.F. Voter, Phys. Rev. B **76**, 205439 (2007).